JOURNAL OF PROPULSION AND POWER
Vol. 17, No. 6, November–December 2001

Newly Developed Direct-Connect High-Enthalpy Supersonic Combustion Research Facility

Mark Gruber,* Jeffrey Donbar,† and Kevin Jackson‡
U.S. Air Force Research Laboratory, Wright–Patterson Air Force Base, Ohio 45433
Tarun Mathur,§ Robert Baurle,¶ and Dean Eklund¶
Taitech, Inc., Beavercreek, Ohio 45430
and
Charles Smith††
Innovative Scientific Solutions, Inc., Dayton, Ohio 45440

A new continuous-flow, direct-connect, high-enthalpy, supersonic combustion research facility is described. This test facility provides combustor inlet flow conditions corresponding to flight Mach numbers between 3.5 and 7, at dynamic pressures up to 95.8 kPa. Most of the major components of the new facility are water cooled (including the vitiated heater, the instrumentation and transition sections, and the facility nozzle and isolators); the current exception is the variable-geometry heat-sink combustor. A variety of conventional and advanced instrumentation, including a steam calorimeter and a thrust stand, exists for accurate documentation of combustor inlet and exit conditions and performance parameters. In a recent calibration effort, pitot pressure surveys, total temperature surveys, and wall static pressure distributions were obtained for a wide range of inlet conditions using Mach 1.8 and 2.2 facility nozzles. In addition, three-dimensional numerical simulations of each test case were completed. Results from the computations compare favorably with experimental results for all cases and yield estimates of the integral boundary-layer properties at the isolator exit.

Nomenclature

A = area
H = facility nozzle exit height
M = Mach number
P = pressure
P_{pitot} = pitot pressure
P_{wall} = wall static pressure
Q = dynamic pressure
T = temperature
U = velocity
x = streamwise coordinate
y = transverse coordinate
γ = specific heat ratio
ΔM, ΔU = percentage difference between simulated and actual Mach number or velocity
δ = boundary-layer thickness based on 99% of average core velocity
δ^* = boundary layer displacement thickness
θ = boundary-layer momentum thickness
ρ = density

Subscripts

act = ramjet performance analysis output condition
ai = aft isolator exit station
B = bottom wall
e = condition at boundary-layer edge
sim = test facility simulation condition
T = top wall
t = stagnation condition
ve = vitiator exit condition
0 = flight condition
4 = facility nozzle exit station
∞ = boundary-layer edge condition

Introduction

SINCE 1995, the Air Force Research Laboratory's Propulsion Directorate, Aerospace Propulsion Office (AFRL/PRA) has been developing a modern, well-characterized, and well-documented direct-connect test facility for full-scale scramjet combustor development. Facility calibration and direct-connect combustor experiments have been underway in this facility since approximately mid-1997.[1–7] The facility provides the Air Force with the opportunity to develop and study unique concepts in supersonic combustor fuel injection, flameholding, ignition, and inlet-combustor isolation, with the ultimate goal of accelerating the development of technologies required for hydrocarbon-fueled dual-mode scramjet propulsion systems. Potential applications for these systems include rapid theater response, global-reach aircraft, and affordable access to space.

The new facility was motivated by several factors. Compared with hydrogen-fueled concepts, the database for hydrocarbon-fueled scramjets is relatively limited. Furthermore, there is a strong need for the Air Force to develop in-house facilities, expertise, and qualified personnel in the areas of high-speed propulsion systems testing and analysis. The goals of the current effort include support of the Hypersonic Technology (HyTech) program[8] (development of a Mach 4–8 hydrocarbon-fueled scramjet missile) and exploration of alternate concepts for improvement of supersonic combustor performance. The facility is designed and developed to perform relatively long-duration, steady-state direct-connect combustor tests. Care is being taken to characterize and accurately document all aspects of this facility. Modern measurement techniques and instrumentation

---

Received 25 April 2001; revision received 10 June 2001; accepted for publication 25 July 2001. This material is declared a work of the U.S. Government and is not subject to copyright protection in the United States.

[*] Aerospace Engineer, Propulsion Directorate, Aerospace Propulsion Office, Building 18, 1950 Fifth Street. Senior Member AIAA.

[†] Aerospace Engineer, Propulsion Directorate, Aerospace Propulsion Office, Building 18, 1950 Fifth Street. Member AIAA.

[‡] Aerospace Engineer, Propulsion Directorate, Aerospace Propulsion Office, Building 18, 1950 Fifth Street; currently with Jackson Design, Beverly Hills, Michigan 48025.

[§] Research Scientist, Innovative Scientific Solutions, Inc., Dayton, Ohio 45440. Member AIAA.

[¶] Research Scientist, 1430 Oak Court, Suite 301. Senior Member AIAA.

[††] Senior Technician, 2766 Indian Ripple Road.

are being incorporated for evaluation of scramjet performance, including thrust-based, chemical-based, and calorimeter-based combustion efficiency.

Facility Description

The following sections describe the testing and simulation capabilities of the new test facility, some details of the various hardware components that comprise the flowpath, and the available instrumentation and control systems. The test cell receives continuous airflow of 13.6 kg/s at 5.17 MPa and a maximum temperature of 922 K with 20.7 kPa continuous exhaust from the Research Air Facility. Both liquid- and gaseous-fuel systems are available, including pumped JP-4, pressurized JP-7, ethylene, and hydrogen. Liquid- and gaseous-oxygen systems are available for makeup oxygen in the vitiated heater. A recirculated cooling-water system provides 158 l/s at 483 kPa; raw dump water at 2.41 MPa is also available. The entire flowpath is secured to a thrust stand for direct measurements of the thrust produced. This measurement may be combined with wall static pressure measurements and a performance analysis code to estimate the combustion efficiency. Additionally, the energy losses through the various water-cooled components, coupled with temperature measurements from a steam calorimeter, allow calculation of combustion efficiency.[9] Additional details regarding the hardware design and fabrication may be obtained elsewhere.[10]

Testing and Simulation Capabilities

Johns Hopkins University/Applied Physics Laboratory's (JHU/APL's) Ramjet Performance Analysis (RJPA)[11,12] code's inlet/diffuser model was used to relate the actual flight conditions of a hypersonic vehicle (and the corresponding combustor inlet conditions) to the test cell operational capabilities and to generate the facility map shown in Fig. 1. This map indicates the range of flight conditions (altitude, Mach number, and dynamic pressure) that can be simulated in the test cell based on the supply air pressure, temperature, and mass flow constraints.

The inlet/diffuser calculations from RJPA were also extended to design the experiments conducted in the test cell. RJPA was executed in an iterative manner such that the following two correlations[13] were simultaneously satisfied for the range of flight simulation conditions presented in Fig. 1 ($3.5 < M_0 < 7$ and $23.9\ \text{kPa} < Q_0 < 95.8\ \text{kPa}$). These calculations yielded predictions of the actual flow properties at the combustor inlet ($T_{4,\text{act}}$, $P_{4,\text{act}}$, $U_{4,\text{act}}$, and $M_{4,\text{act}}$) at each flight condition assuming the inlet of the hypersonic vehicle varies to satisfy Eqs. (1) and (2), that is, the inlet is optimized for each flight Mach number.

$$(A_0/A_4) = -3.5 + 2.17M_0 - 0.017M_0^2 \tag{1}$$

$$(P_4/P_0) = -8.4 + 3.5M_0 + 0.63M_0^2 \tag{2}$$

In the direct-connect test facility, four facility nozzles (with design Mach numbers of 1.8, 2.2, 2.6, and 3.0) are available to establish the conditions entering the combustor. If the vitiated airflow through the nozzle is assumed to be isentropic with a specific heat ratio of $\gamma_4 = 1.3$, then the facility stagnation conditions may be computed such that the static temperature and pressure entering the combustor match those determined using RJPA ($T_{4,\text{sim}} = T_{4,\text{act}}$ and $P_{4,\text{sim}} = P_{4,\text{act}}$, respectively). Table 1 presents a summary of the simulation capabilities using the various facility nozzles. Table 1 also shows how well the combustor Mach number and velocity obtained using the available nozzles compare with the values calculated using RJPA. The conditions where each facility nozzle operates on-design, (that is, actual values of T_4, P_4, M_4, and U_4 closely match the RJPA output) are noted. Because each facility nozzle can exactly match all parameters at only one condition, compromises will exist in both

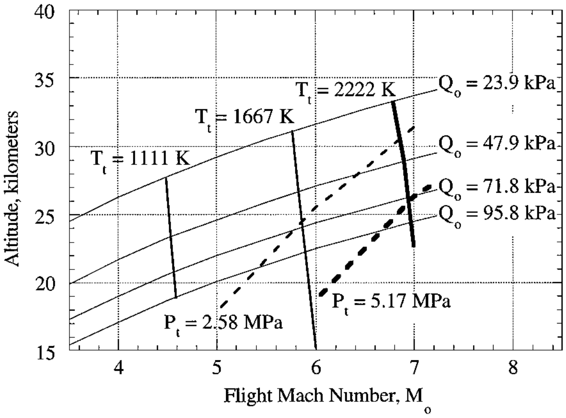

Fig. 1 Test cell 22 facility map.

Table 1 Facility test conditions using $\gamma_4 = 1.3$ and forcing $T_{4,\text{sim}} = T_{4,\text{act}}$ and $P_{4,\text{sim}} = P_{4,\text{act}}$

M_0	Q_0, kPa	$M_{4,\text{act}}$	$M_{4,\text{sim}}$	$T_{4,\text{sim}}$, K	$P_{4,\text{sim}}$, kPa	$U_{4,\text{sim}}$, m/s	ΔM_4, %	ΔU_4, %
3.5[a]	23.9[a]	1.74[a]	1.80[a]	478[a]	31.8[a]	760[a]	3.2[a]	0.0[a]
3.5[a]	47.9[a]	1.74[a]	1.80[a]	468[a]	64.6[a]	753[a]	3.2[a]	0.0[a]
3.5[a]	95.8[a]	1.74[a]	1.80[a]	468[a]	132.4[a]	753[a]	3.2[a]	0.0[a]
4.0	23.9	1.96	1.80	533	32.8	803	−8.3	−11.0
4.0	47.9	1.96	1.80	523	66.3	795	−8.3	−10.9
4.0	95.8	1.96	1.80	519	126.8	793	−8.3	−10.8
4.5[a]	23.9[a]	2.17[a]	2.20[a]	588[a]	33.3[a]	1031[a]	1.4[a]	−1.4[a]
4.5[a]	47.9[a]	2.17[a]	2.20[a]	577[a]	67.0[a]	1021[a]	1.4[a]	−1.5[a]
4.5[a]	95.8[a]	2.17[a]	2.20[a]	568[a]	136.8[a]	1014[a]	1.4[a]	−1.5[a]
5.0	23.9	2.39	2.20	641	33.4	1076	−7.8	−10.0
5.0	47.9	2.39	2.20	628	66.7	1065	−7.8	−10.2
5.0	95.8	2.39	2.20	616	134.9	1055	−7.8	−10.1
5.5	23.9	2.59	2.60	693	33.3	1323	0.5	−1.8
5.5	47.9	2.59	2.60	679	66.4	1310	0.5	−1.9
5.5	95.8	2.59	2.60	666	134.3	1296	0.5	−1.9
6.0	23.9	2.79	2.60	744	33.3	1370	−6.7	−8.7
6.0	47.9	2.79	2.60	730	65.7	1357	−6.7	−8.7
6.0	95.8	2.79	2.60	715	133.4	1343	−6.7	−8.8
6.5[a]	23.9[a]	2.98[a]	3.00[a]	796[a]	32.8[a]	1636[a]	0.6[a]	−1.4[a]
6.5[a]	47.9[a]	2.98[a]	3.00[a]	777[a]	64.9[a]	1616[a]	0.6[a]	−1.5[a]
6.5[a]	95.8[a]	2.98[a]	3.00[a]	762[a]	130.3[a]	1600[a]	0.6[a]	−1.5[a]
7.0	23.9	3.17	3.00	853	32.7	1694	−5.2	−6.9
7.0	47.9	3.17	3.00	828	64.4	1668	−5.2	−7.0
7.0	95.8	3.17	3.00	811	128.9	1651	−5.2	−7.0

[a] Actual values closely match RJPA output.

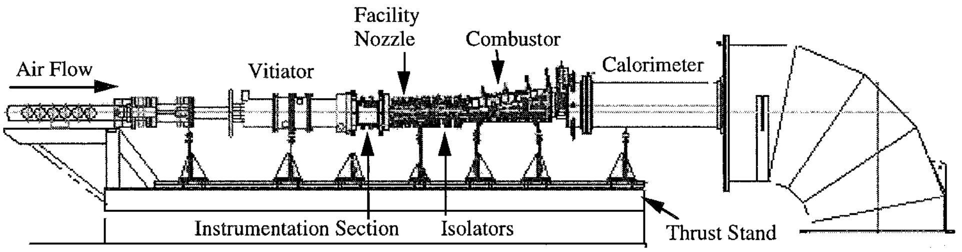

Fig. 2 Facility schematic.

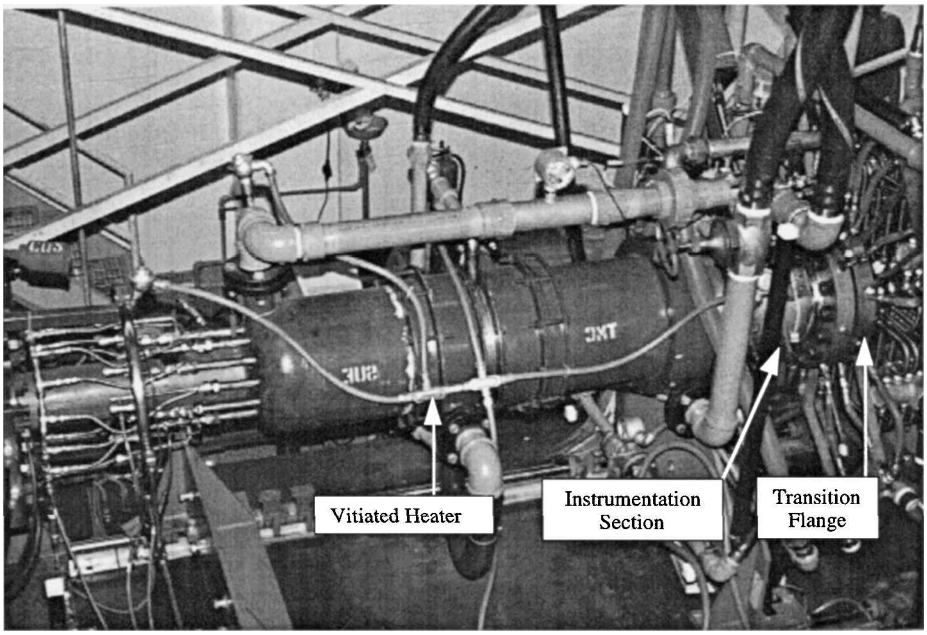

Fig. 3 Test cell 22 hardware, upstream.

Mach number and velocity if the nozzle is operated at conditions away from that design point.

Hardware

Figure 2 is a schematic of the facility with flow from left to right. Supply air enters a modified Marquardt sudden expansion (SuE) vitiator capable of sustaining temperatures to about 2500 K. The vitiator is fitted with an igniter system (H_2/air) and can be fueled with both liquid and gaseous fuels. For the tests described here, JP-4 was used to fuel the vitiator. A water-cooled instrumentation section placed downstream of the vitiator permits stagnation temperature and/or pressure measurements with traversing probes, wall static pressure/gas sampling ports, and eight thermocouple ports in the inlet and outlet flanges. A water-cooled transition flange compresses the vitiated airflow from axisymmetric (254 mm i.d.) to two dimensional (57.2 × 177.8 mm) as it enters the facility nozzle. These components appear in the photograph shown in Fig. 3.

Four interchangeable water-cooled facility nozzles are available to expand the air to supersonic conditions, simulating desired combustor inlet flow conditions. The nozzle section has 23 static pressure taps on its side wall for documenting the axial static pressure profile from the nozzle inlet to exit. Two removable isolator sections downstream of the nozzle (water cooled, each 305 mm long with a total of 120 static pressure taps on top and bottom walls) are used to contain the precombustion pressure rise. The isolator sections incorporate a 0.75-deg divergence along the bottom wall to compensate for boundary-layer growth.

Immediately following the isolator sections is a variable-geometry heat-sink combustor with a flexible upper wall currently set to provide an area ratio of approximately 2.5. The combustor also has removable inserts on all four walls, allowing optical access and installation of a variety of instrumentation. The replaceable inserts provide a wide parametric design space for fuel injection and flameholding concepts. The initial configuration incorporates four low-angle (15 deg) flush-wall fuel injectors upstream of a cavity-based flameholder.[2,3] Liquid and gaseous hydrocarbon fuels are available for the combustor. An air throttle is available to facilitate combustor ignition. The air throttle supplies controlled quantities of compressed air into the combustor at a desired axial station. Its duration is variable (minimum of approximately 2 s); a typical cycle involves between 4 and 10 s of airflow.

A calorimeter instrumentation section that houses water sprays, rakes, and probes connects the combustor to a calorimeter instrumented with thermocouples and heat-flux gauges. The calorimeter exit connects to an elbow through which the flow exits the test cell to an exhauster system. The photograph in Fig. 4 shows the combustor, calorimeter instrumentation, and calorimeter sections.

The test hardware also includes a spray-cooled, carbon–steel calibration section that can be attached to the exit of the facility nozzle or either isolator. This section has ports for water-cooled traversing probes, allowing spanwise and transverse total temperature and pitot pressure surveys at the nozzle and/or isolator exit planes. This device incorporates a sudden area change at the probe station so that the probe may be positioned above and below the actual top and bottom walls. The attachment of this section to the exit of either isolator results in the formation of a weak compression wave from the bottom wall as the flow turns through 0.75 deg toward the rig centerline. A remotely actuated butterfly valve installed downstream of this section permits studies of a simulated precombustion shock train positioned in the facility isolator sections.

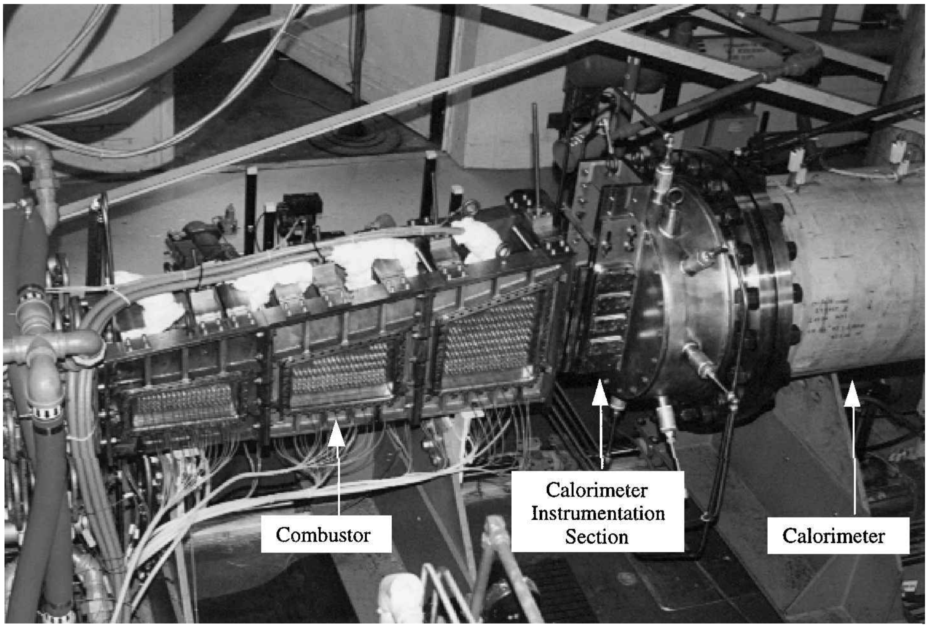

Fig. 4 Test cell 22 hardware, downstream.

Instrumentation

A CAMAC process I/O system is used for both data acquisition and process control. Two Sun 630MP workstations serve as the data acquisition and facility control systems. The data acquisition system has 416 channels of analog input, 64 channels of digital I/O, and 40 channels of analog output. The CAMAC crates are connected to the two workstations via a fiber optic small computer system SCSI interface. A Pressure Systems, Inc. (PSI) 8400 pressure scanning system currently consisting of 400 channels with real-time display and data reduction is also available.

Total mass flow rate through the rig at each test condition is estimated using two independent methods. The first method sums the flow rates of facility air, vitiator fuel, and makeup oxygen, measured using an orifice plate and two turbine meters, respectively. The second method uses the stagnation pressure and temperature measurements in the instrumentation section, the known facility nozzle throat area, and simple one-dimensional gasdynamic relations. The close correspondence between these two estimates, generally within 1–3%, inspires confidence in the quality and reliability of instrumentation and analysis in the test cell. Stagnation temperature is currently measured using thermocouples (for temperatures up to around 1200 K).

Remote monitoring of test activities is provided by five video cameras placed at strategic locations throughout the test cell. Four cameras placed around the thrust stand monitored the facility hardware. A hand-held Sony 8-mm camera monitored the traversing probe.

Calibration Efforts

Experimental and numerical studies were conducted to calibrate two facility nozzles (Mach 1.8 and 2.2) in conjunction with the isolator sections. Table 2 presents the stagnation conditions corresponding to the 12 calibration cases examined. The following sections describe the experimental and computational methods used to diagnose the flowfield and the results of the calibration studies. For brevity, results from one case for each facility nozzle (cases 1 and 9) are presented in this paper.

Experimental Details

Two separate water-cooled traversing probes were used for hardware calibration. The first probe contained eight pitot pressure tips covering approximately 25 mm in the spanwise direction. The second probe consisted of four pitot pressure tips and two total temperature tips over the same span. The pitot pressure tips were made from hypodermic tubing (0.53 mm i.d.). Total temperatures were measured using fine gauge thermocouples set inside aspirated ceramic diffusers.[14] Both probes were inserted into the calibration section from the top and were connected to a computer-controlled electronic actuator for remote positioning. Pressures were measured using the PSI system while the thermocouple signals were recorded via the CAMAC data acquisition system.

Table 2 Experimental and computational calibration test conditions

Case	$M_{4,\mathrm{act}}$	T_{ve}, K	P_t, kPa	P_{ai}/P_4
1	1.8	833	372	0.97, 2.78, 3.52
2	1.8	778	703	0.94, 2.76, 3.54
3	1.8	972	372	0.96, 2.72, 3.51
4	1.8	917	752	0.94, 2.84, 3.49
5	1.8	1139	365	0.96, 2.59, 3.34
6	1.8	1083	745	0.94, 2.51, 3.50
7	2.2	902	689	0.94, 2.55, 4.46
8	2.2	917	1351	0.92, 3.12, 4.05
9	2.2	1083	710	0.94, 3.00, 4.50
10	2.2	1063	1441	0.92, 3.05, 3.86
11	2.2	1259	703	0.93, 2.65, 4.35
12	2.2	1232	1420	0.92, 3.04, 3.93

Computational Details

Three-dimensional simulations were performed at low backpressure for each of the 12 cases outlined in Table 2. These computations provide results for comparison with the experimental measurements. The computational results provide a suitable means for calculating the boundary-layer properties (boundary-layer thickness δ, the displacement thickness

$$\delta^* = \int_0^\infty \left(1 - \frac{\rho}{\rho_e}\frac{U}{U_e}\right) \mathrm{d}y \tag{3}$$

and the momentum thickness

$$\theta = \int_0^\infty \frac{\rho}{\rho_e}\frac{U}{U_e}\left(1 - \frac{U}{U_e}\right) \mathrm{d}y \tag{4}$$

at the isolator exit plane. Additional simulations were performed at elevated backpressures for cases 1 and 9. The method used to calculate the flowfields at low backpressure will first be described followed by modifications employed for the elevated back-pressure simulations.

The computational domain included the subsonic and supersonic portions of the nozzle, the isolator, and the 47.6-mm-long constant area calibration section that was attached at the end of the isolator. Spanwise symmetry was assumed; hence, the domain extended from the tunnel centerline to the side wall in the spanwise direction. The calculations were performed with the VULCAN Navier–Stokes code,[15] a derivative of the LARCK code developed at NASA Langley Research Center. The calculations employed the low-diffusion flux vector split scheme of Edwards[16] for the evaluation of the inviscid fluxes. The MUSCL parameter was set to one-third to minimize truncation error. The thin-layer viscous terms were computed in the three coordinate directions. Turbulence was modeled with the Menter[17] two-equation BSL turbulence model. At solid surfaces, the wall-matching procedure of Wilcox[18] was employed to reduce grid requirements. The turbulent Prandtl number was set to 0.89. The subsonic portion of the nozzle extended a short distance downstream of the throat and was solved elliptically, whereas the sections downstream were solved with the space marching algorithm.

The simulated vitiated airstream composition was obtained from the experimental flow rate measurements assuming complete combustion. The resulting mass fractions of N_2, O_2, CO_2, and H_2O were 0.722, 0.232, 0.033, and 0.013 for case 1 and 0.688, 0.232, 0.058, and 0.022 for case 9, respectively. The calculations were performed with a single species that had the molecular weight and thermodynamic coefficients set equal to the vitiated heated air mixture values.

The inflow boundary was prescribed by fixing the stagnation pressure and temperature. The stagnation temperature at the inflow of the nozzle was obtained by adjusting the measured temperature at the exit of the vitiated heater for the heat loss through the instrumentation and transition sections. The nozzle inflow total temperatures for cases 1 and 9 were 815 and 1058 K, respectively. The outflow boundary condition for the elliptic region was first-order extrapolation. The top, bottom, and side walls employed a no-slip isothermal boundary condition. The wall temperature in the nozzle and isolator sections was determined by iteratively performing a series of two-dimensional calculations until the calculated heat loss matched the experimentally measured heat loss. These wall temperatures were then imposed on the three-dimensional calculations. The measured heat loss exceeded the heat loss resulting from each three-dimensional calculation by less than 5%. The calibration section was cooled to an unknown extent. In these simulations, the calculated heat loss through this section was slightly overpredicted, thereby compensating, to some extent, the underpredicted heat loss in the nozzle and isolator sections. The resulting nozzle and isolator wall temperatures were 400 and 330 K, respectively, for case 1, and 455 and 380 K, respectively, for case 9. Finally, a symmetry boundary condition (zero spanwise velocity component and extrapolation of all other flow quantities) was employed along the centerline plane.

The calculations were advanced in time with a diagonalized approximate factorization scheme[19] with the Courant–Friedrichs–Lewy (CFL) number set equal to 4.0 and 5.0 for the elliptic and space marching regions, respectively. The convergence criterion employed was a relative error of the $L2$ norm of the residual of 10^{-6}. The mass flow conservation was excellent; mass loss did not exceed 0.3%.

A sensitivity study was conducted for case 1 using three different grids. The coarsest grid had 171 points in the axial direction, 40 points in the transverse direction, and 22 points in the spanwise direction ($171 \times 40 \times 22$). The finest grid doubled the number of points in each direction, that is, $341 \times 79 \times 43$, whereas the intermediate grid only doubled the number of points in the axial and transverse directions, that is, $341 \times 79 \times 22$. Increasing the grid density in the axial direction provided better resolution of the weak pressure waves in the nozzle and isolators, whereas coarse resolution in the transverse direction yielded thicker boundary layers. The solutions obtained using the intermediate and finest grids were examined on the rig centerline. Results were found to be nearly indistinguishable. Consequently, the calculations for the remaining cases employed the intermediate grid to reduce computational time. Figure 5 shows the computational grid along the rig centerline for the Mach 1.8 facility nozzle (every other point has been removed for clarity). The calculated Mach number contours along the rig centerline for case 1 appear in Fig. 6. This plot indicates that the nozzle performs as designed with an exit Mach number near 1.8.

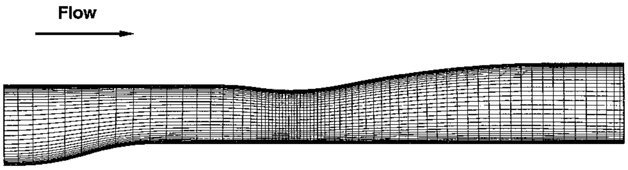

Fig. 5 Computational grid for Mach 1.8 facility nozzle (every other point removed).

Fig. 6 Mach number contours from Mach 1.8 facility nozzle calculation.

Additionally, calculations were performed with elevated backpressures at the exit plane of the calibration section for cases 1 and 9. The isolator and calibration sections were solved together elliptically with the flow variables at the inflow boundary set equal to the calculated values at the exit plane of the nozzle, and all flow variables at the outflow boundary extrapolated from the interior (except for the pressure, which was imposed). Only results from the highest backpressure condition will be presented because a significant region of reverse flow was present at the outflow plane for the intermediate backpressure condition. At the highest backpressure condition for case 9, reverse flow was present in a small region in the corner of the duct that represented approximately 0.03 and 0.40% of the exit area on the coarse and fine grids, respectively. This should have a minimal impact on the results. The pressure rise for the highest backpressure condition for case 1 extended into the nozzle, and consequently, the section of the nozzle downstream of the throat was included in the elliptic solution domain. The wall temperature was assumed to be the same as in the nonbackpressured simulations. The thin-layer approximation for the viscous terms was not employed in the simulations with an imposed backpressure. Solutions were obtained on the fine grid ($341 \times 79 \times 43$) that had additional points in the spanwise direction to resolve the recirculation zone along the side wall. Solutions were also obtained on a coarse grid with every other grid point removed in each coordinate direction ($171 \times 40 \times 22$) to investigate the grid sensitivity of the results. The $L2$ norm of the residual in the solutions with an imposed backpressure dropped approximately three orders of magnitude. Convergence was assessed, practically, by monitoring changes in mass-weighted one-dimensional quantities. Convergence was considered adequate when mass-weighted one-dimensional quantities did not change after 5000 iterations.

Mach 1.8 Facility Nozzle Results

Figures 7–11 present the results of the Mach 1.8 nozzle calibrations for case 1. Wall static pressures through the nozzle and isolator sections appear in Fig. 7. Included in this plot are all of the measured pressures, the data obtained from the numerical simulation, and a theoretical pressure distribution based on a one-dimensional isentropic analysis. The axial position is scaled by the nozzle exit height, and $x/H = 0$ corresponds to the facility nozzle exit plane. The pressure data are normalized by the nozzle exit pressure P_4. With low backpressure, static pressure profiles through the nozzle and isolator sections match the isentropic prediction and the numerical simulation. As the downstream valve is closed, the pressure at the isolator exit rises, resulting in a system of shock waves. This shock

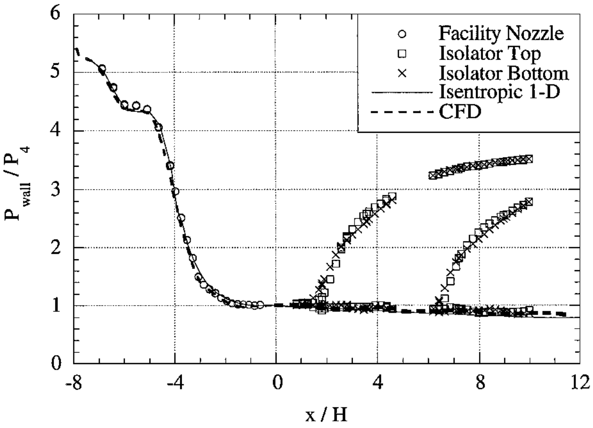

a) Case 1 with three levels of backpressure

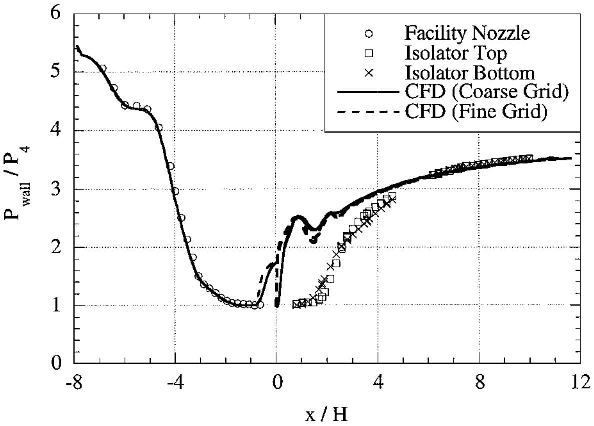

b) Comparison of CFD coarse and fine grid solutions for case 1 ($P_{ai}/P_4 = 3.52$)

Fig. 7 Normalized wall static pressure distributions with Mach 1.8 facility nozzle.

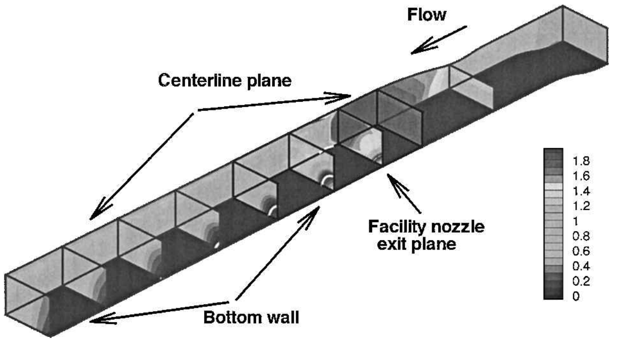

Fig. 8 Calculated Mach number contours from case 1 at $P_{ai}/P_4 = 3.52$ (zero streamwise velocity indicated by a white line).

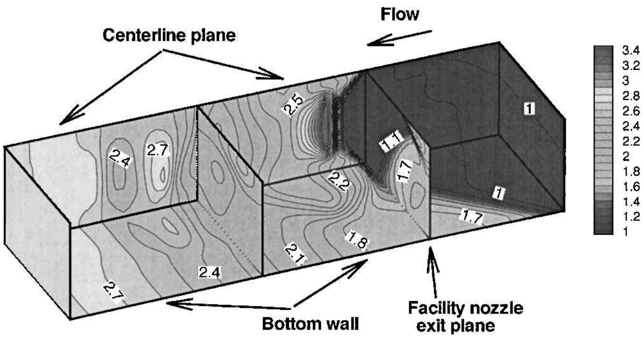

Fig. 9 Calculated normalized static pressure contours from case 1 at $P_{ai}/P_4 = 3.52$ in the vicinity of the shock train.

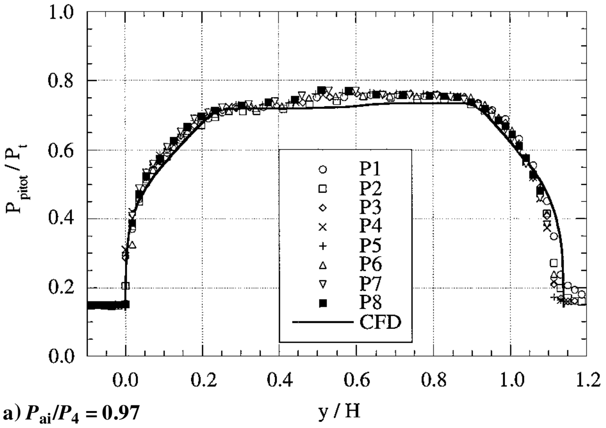

a) $P_{ai}/P_4 = 0.97$

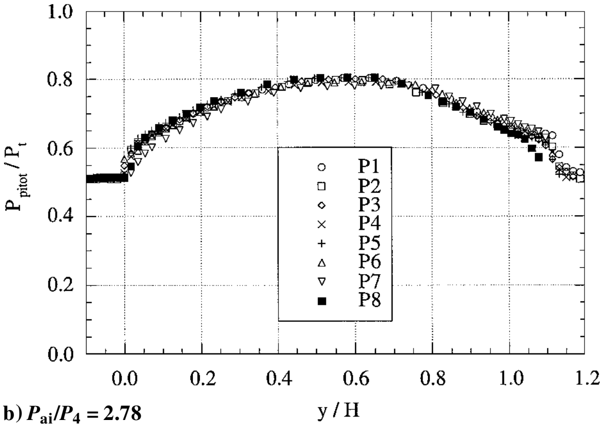

b) $P_{ai}/P_4 = 2.78$

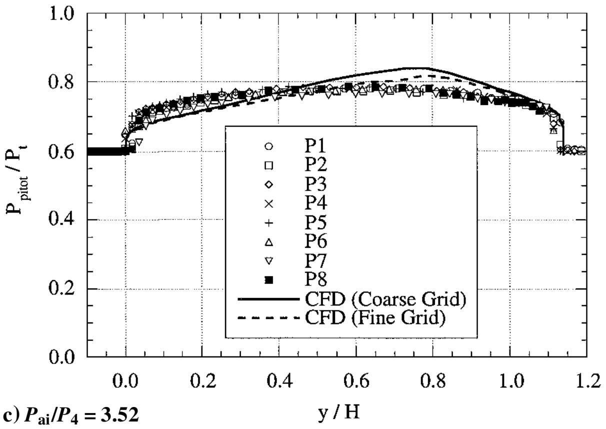

c) $P_{ai}/P_4 = 3.52$

Fig. 10 Normalized isolator exit plane pitot pressure distributions from case 1.

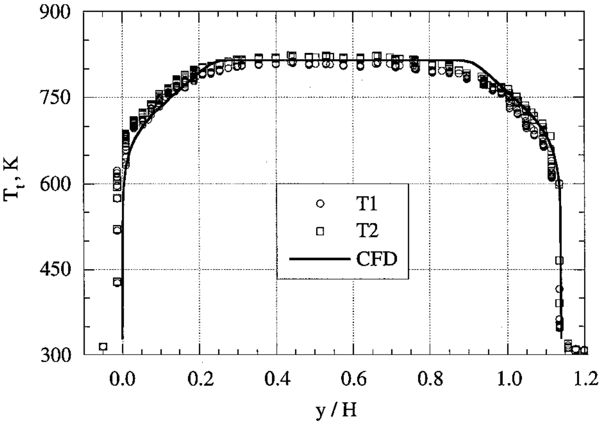

Fig. 11 Normalized isolator exit plane total temperature distributions from case 1 at $P_{ai}/P_4 = 0.97$.

system decelerates the approaching flow. Figure 7a contains measured static pressure distributions for two levels of increased backpressure, $P_{ai}/P_4 = 2.78$ and 3.52. The pressures along the top and bottom walls of the isolator sections are very similar in each profile. As expected, increased exit pressure forces the shock train upstream. These distributions illustrate the effectiveness of the isolators in containing a combustor pressure rise that is nearly equivalent to a normal shock.

The computational fluid dynamics (CFD) prediction at the higher backpressure condition are shown in Fig. 7b along with the measured pressure data from this condition. Along the centerline plane, the pressure rise from the shock train begins at $x/H = 0$, which is approximately 1.5 duct heights upstream of the measured location for the beginning of the pressure rise. The flow separates initially in the corner between the side wall and the bottom wall; the corresponding oblique shock causes the pressure rise to occur farther upstream on the side wall than along the centerline plane. Downstream of the nearly normal shock along the centerline plane, there is a series of expansion and compression waves causing the pressure to decrease and increase. A steady solution was obtained computationally. The monotonic rise in the measured wall pressures downstream of the shock may be due to flow unsteadiness and a consequent averaging of the crests and troughs in the pressure values. The shock position and overall character of the flow is represented well by the coarse grid solution, although the flow quantities are more diffuse due to numerical dissipation.

Figure 8 shows the Mach number contours along the centerline plane and several crossflow planes for the solution obtained on the fine grid. The contour of zero streamwise velocity is overlaid in white to identify the boundary of the recirculation zone, which emanates from the corner of the side wall and bottom wall and extends 11.0 duct heights from $-1.2 < x/H < 9.8$. For comparison, the recirculation zone in the coarse grid solution extended 9.4 duct heights ($-0.9 < x/H < 8.5$). At the exit of the domain the Mach number distribution retains a significant spanwise variation with lower momentum flow toward the side wall. The domain extending from $-1.4 < x/H < 3.7$ is outlined in black. The pressure contours for this region appear in Fig. 9. The peak pressure ratio along the centerline plane is $P_{ai}/P_4 = 3.57$, which corresponds to 97% of the normal shock pressure rise as determined from the local values of the pressure, Mach number, and ratio of specific heats for the flow upstream of the shock. The footprint of the oblique shock generated by the flow disturbance from the recirculation zone formed in the duct corner is observed on the bottom wall. The pressure rise along the bottom and side wall extends slightly over one duct height upstream of the shock position along the tunnel centerline. The reflection of the oblique shock off the top wall of the duct can also be seen at the exit plane of the nozzle. While the flow in this region is highly three dimensional, the pressure field downstream of this region is essentially one dimensional, as observed in the downstream crossflow plane in Fig. 9.

Figure 10 shows the pitot probe measurements obtained just downstream of the aft isolator exit for each of the three backpressure levels examined. In Figs. 10a–10c the transverse position is scaled by the facility nozzle exit height, and $y/H = 0$ corresponds to the top wall of the isolator. The pitot pressures are normalized by the facility stagnation pressure. Figure 10a presents the experimental and numerical results obtained from case 1 at low backpressure. The eight measured pressures are very consistent across the duct height for all cases examined. The computed profile compares well with the measured values. Figures 10b and 10c contain normalized pitot pressures at $P_{ai}/P_4 = 2.78$ and 3.52, respectively. These profiles again exhibit a high degree of consistency from one probe tip to another. They also illustrate the effect of the shock train on the overall flowfield. At the highest backpressure level, the flow exiting the aft isolator is purely subsonic. The CFD results shown in Fig. 10c suggest that the shock train is somewhat asymmetric from top to bottom. Shock train unsteadiness is one possible cause for these differences. The experimental data represent averages over a relatively long time (and potentially many oscillation cycles), and the CFD solution is steady in nature.

Total temperature measurements appear in Fig. 11 for case 1 operated at the low backpressure condition. CFD results are overlaid on the measurements and compare very well across the duct height. This plot suggests that the core flow is not strongly affected by the heat loss through the water-cooled sections (T_{ve} for case 1 is 833 K).

Mach 2.2 Facility Nozzle Results

Figures 12–14 contain results of the Mach 2.2 nozzle calibrations for case 9 (refer to Table 2). The measured, calculated, and isentropic wall static pressure distributions shown in Fig. 12a compare very favorably. As with the Mach 1.8 results (Fig. 7), increased

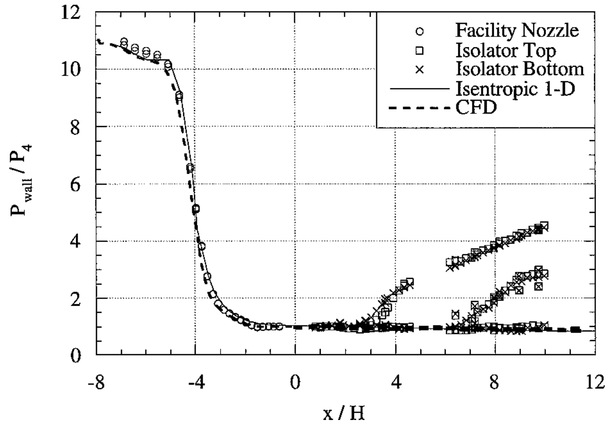

a) Case 9 with three levels of backpressure

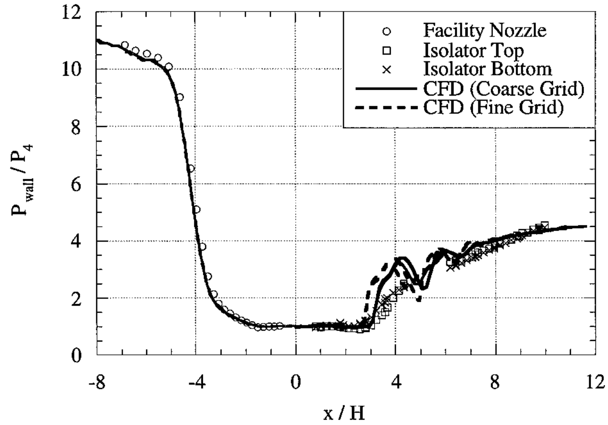

b) Comparison of CFD coarse and fine grid solutions for case 1 ($P_{ai}/P_4 = 4.50$)

Fig. 12 Normalized wall static pressure distributions with Mach 2.2 facility nozzle.

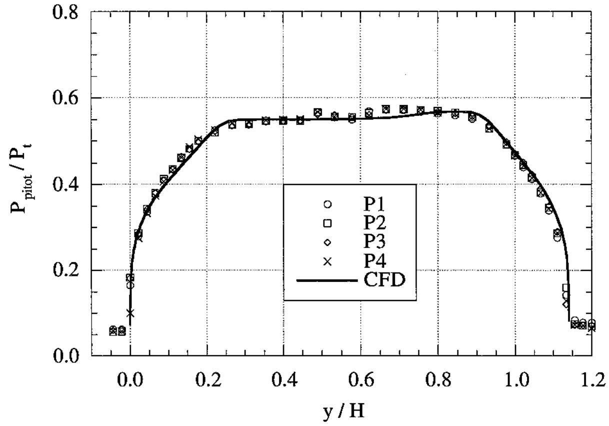

Fig. 13 Normalized isolator exit plane pitot pressure distributions from case 9 at $P_{ai}/P_4 = 0.94$.

Table 3 Integral boundary-layer properties at aft isolator exit plane

Case	Unit Reynolds no., m^{-1}	δ_T, δ_B, mm	δ^*_T, δ^*_B, mm	θ_T, θ_B, mm	δ_T/δ^*_T, δ_B/δ^*_B	δ_T/θ_T, δ_B/θ_B	δ^*_T/θ_T, δ^*_B/θ_B
1	12.1×10^6	12.7, 12.3	1.62, 1.60	1.35, 1.29	7.8, 7.7	9.4, 9.5	1.2, 1.2
2	25.3×10^6	12.0, 11.4	1.57, 1.50	1.19, 1.12	7.6, 7.6	10.1, 10.2	1.3, 1.3
3	10.2×10^6	13.1, 12.6	1.52, 1.52	1.42, 1.37	8.6, 8.3	9.2, 9.2	1.1, 1.1
4	22.0×10^6	12.3, 11.8	1.47, 1.42	1.27, 1.19	8.4, 8.3	9.7, 9.9	1.2, 1.2
5	8.2×10^6	13.4, 13.1	1.40, 1.37	1.55, 1.50	9.6, 9.6	8.6, 8.7	0.9, 0.9
6	17.7×10^6	12.5, 12.1	1.37, 1.35	1.37, 1.29	9.1, 9.0	9.1, 9.4	1.0, 1.0
7	16.4×10^6	12.2, 12.2	1.85, 1.93	1.22, 1.19	6.6, 6.3	10.0, 10.3	1.5,1.62
8	31.2×10^6	11.6, 11.5	1.73, 1.78	1.12, 1.09	6.7, 6.5	10.4, 10.6	1.5, 1.6
9	13.1×10^6	12.6, 12.6	1.83, 1.88	1.32, 1.30	6.9, 6.7	9.5, 9.7	1.4, 1.4
10	26.9×10^6	11.9, 11.9	1.68, 1.75	1.17, 1.14	7.1, 6.8	10.2, 10.4	1.4, 1.5
11	10.8×10^6	13.2, 13.3	1.68, 1.75	1.42, 1.42	7.8, 7.6	9.3, 9.4	1.2, 1.2
12	22.3×10^6	12.3, 12.3	1.57, 1.62	1.27, 1.24	7.8, 7.6	9.7, 9.9	1.2, 1.3

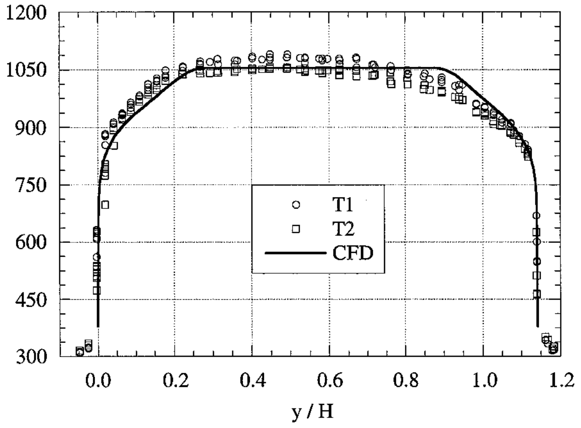

Fig. 14 Normalized isolator exit plane total temperature distributions from case 9 at $P_{ai}/P_4 = 0.94$.

backpressure results in the formation of a system of shock waves positioned in the isolator sections. Increasing backpressure forces this disturbance upstream. At this inlet Mach number, the isolator sections effectively contain a pressure ratio of $P_{ai}/P_4 = 4.50$.

The CFD pressure data at the higher backpressure condition are shown in Fig. 12b along with the measured pressure data from this condition. There is good agreement between the CFD and measured data regarding the position of the pressure rise, although a small grid sensitivity is observed. As with the Mach 1.8 nozzle, the pressure distribution in the coarse grid solution is more diffuse than in the fine grid solution, whereas the measurements exhibit a monotonic pressure rise.

Figure 13 shows the measured and computed pitot pressure distributions from just downstream of the aft isolator exit for case 9 operated at low backpressure. For these measurements, the probe with four pitot tubes was used. All four sets of measurements agree closely across the entire duct height. Also, the numerical results reproduce the features of the measured profile very well, including the weak compression wave that elevates the pitot pressure near the bottom wall ($0.7 < y/H < 0.9$). The pitot pressure distributions in the top and bottom wall boundary layers are well represented by the CFD results.

Finally, Fig. 14 shows the measured and calculated total temperature distributions from case 9 operated at low backpressure. As in the Mach 1.8 nozzle results, the measured and computed total temperature distributions compare very favorably across the duct height. Again, the water-cooled hardware does not strongly influence the total temperature of the core flow (T_{ve} for case 9 is 1083 K).

Integral Boundary-Layer Properties

Based on the good agreement between the CFD results and measured quantities, the calculated profiles were used to determine the integral boundary-layer properties at the isolator exit plane along the rig centerline for each of the 12 cases. The trapezoidal method was used for numerical integration. Velocity and density values were obtained at the cell center location, and the grid coordinates were obtained from the computational grid. The boundary-layer properties were found to be quite sensitive to the choice of the edge velocity U_e. To minimize any subjectivity, the average velocity in the region of the core flow where $\mathrm{d}U/\mathrm{d}y < 500\ \mathrm{s}^{-1}$ was defined as U_∞, and the edge velocity was defined as $U_e = 0.99 \times U_\infty$. The results of the integration process are tabulated in Table 3.

The trends in the calculated values for δ^* and θ can largely be explained by considering the distribution of ρ/ρ_e. For a given distribution of U/U_e, an increase in ρ/ρ_e reduces δ^*, the effective distance occupied by the boundary layer, and increases θ, the associated drag force on a flat plate. In the simulations using a fixed Mach number nozzle, ρ/ρ_e increases as the total temperature increases due to the corresponding increase in heat transfer to the walls of the water-cooled hardware. Consequently, larger values are obtained for θ as the total temperature increases. The unit Reynolds number decreases with increasing total temperature, resulting in an increase in δ and a decrease in U/U_e at a fixed distance from the wall. Finally, the increase in ρ/ρ_e is larger than the reduction in U/U_e, resulting in a reduction in δ^* with increased total temperature.

Summary

A newly developed supersonic combustion research facility has been described. This test facility offers a broad flight Mach number and dynamic pressure simulation space using four interchangeable facility nozzles. The major components of the rig are water-cooled for exposure to relatively long test times to allow for steady-state measurements of combustor performance. Modern data acquisition and control systems are available, along with a variety of optical diagnostic techniques for documentation of crucial combustor performance parameters including the inlet conditions, thrust, combustion efficiency, combustor heat loss, and wall static pressures. The results of a recent effort to calibrate two of the facility nozzles demonstrate that the nozzle and isolator sections perform as expected. Wall static pressure distributions show the effectiveness of the isolator sections at containing a simulated precombustion shock train. CFD results compare well with the wall and in-stream measurements. These results have been analyzed to obtain integral boundary-layer properties at the aft isolator exit plane.

Acknowledgments

The U.S. Air Force Hypersonic Technology Program, under the guidance of R. Mercier, provided the funding for this work. The authors thank F. Billig and T. Jackson for their technical guidance; J. Bryant, M. Cox, W. Haendiges, and G. Streby for technical support of the test facility; and W. Eakins, G. Haines, and P. Saunders for detailed design of the hardware. The support of the Research Air Facility is also appreciated.

References

[1] Jackson, K., Gruber, M., Mathur, T., Streby, G., Smith, C., and Billig, F., "Calibration of a Newly Developed Direct-Connect High-Enthalpy Supersonic Combustion Research Facility," AIAA Paper 98-1510, April 1998.

[2] Mathur, T., Streby, G., Gruber, M., Jackson, K., Donbar, J., Donaldson, W., Jackson, T., Smith, C., and Billig, F., "Supersonic Combustion Experiments with a Cavity-Based Fuel Injector," AIAA Paper 99-2102, June 1999.

[3] Gruber, M., Jackson, K., Mathur, T., and Billig, F., "Experiments with a Cavity-Based Fuel Injector for Scramjet Applications," International Symposium on Air Breathing Engines, ISABE Paper IS-7154, Sept. 1999.

[4] Gruber, M., Donbar, J., Jackson, T., Mathur, T., Eklund, D., and Billig, F., "Performance of an Aerodynamic Ramp Fuel Injector in a Scramjet Combustor," AIAA Paper 2000-3708, July 2000.

[5] Mathur, T., Lin, K.-C., Kennedy, P. J., Gruber, M. R., Donbar, J. M., Jackson, T. A., and Billig, F. S., "Liquid JP-7 Combustion in a Scramjet Combustor," AIAA Paper 2000-3581, July 2000.

[6] Donbar, J. M., Gruber, M. R., Jackson, T. A., Carter, C. D., and Mathur, T., "OH PLIF Imaging in a Hydrocarbon-Fueled Scramjet Combustor," *Proceedings of the Twenty-Eighth International Symposium on Combustion*, Combustion Inst., Pittsburgh, PA, 2000, pp. 679–687.

[7] Mathur, T., Gruber, M., Jackson, K., Donbar, J., Donaldson, W., Jackson, T., and Billig, F., "Supersonic Combustion Experiments with a Cavity-Based Fuel Injector," *Journal of Propulsion and Power*, Vol. 17, No. 6, 2001, pp. 1305–1312.

[8] Mercier, R. A., and Ronald, T. M. F., "Hypersonic Technology (HyTech) Program Overview," AIAA Paper 98-1566, Nov. 1998.

[9] Thompson, M. W., "Equilibrium Chemistry Steam Calorimetry Data Analysis Procedure Using the Ramjet Performance Analysis Code," Johns Hopkins Univ./Applied Physics Lab., Rept. RTDC-TPS-028, Baltimore, MD, 1997.

[10] Streby, G. D., Mathur, T., Chen, T. H., and Eakins, W. E., "Advanced Airbreathing Hydrocarbon-Fueled Aero-Engine Concepts," Air Force Research Lab., Rept. AFRL-PR-WP-TR-1999-2038, Wright–Patterson AFB, OH, 1999.

[11] Pandolfini, P. P., Billig, F. S., Corpening, G. P., Corda, S., and Friedman, M. A., "Analyzing Hypersonic Engines Using the Ramjet Performance Analysis Code," *APL Technical Review*, Vol. 2, No. 1, 1990, pp. 68–79.

[12] Pandolfini, P. P., and Friedman, M. A., "Instructions for Using Ramjet Performance Analysis (RJPA)—IBM-PC Version 1.24," Johns Hopkins Univ./Applied Physics Lab., Rept. AL-92-P175, Baltimore, MD, 1992.

[13] Billig, F. S., "Research on Supersonic Combustion," *Journal of Propulsion and Power*, Vol. 9, No. 4, 1993, pp. 499–514.

[14] Winkler, E. M., "Design and Calibration of Stagnation Temperature Probes for Use at High Supersonic Speeds and Elevated Temperatures," *Journal of Applied Physics*, Vol. 25, 1954, pp. 231–238.

[15] White, J., "A Pseudo-Temporal Multi-Grid Relaxation Scheme for Solving the Parabolized Navier–Stokes Equations," AIAA Paper 99-3360, June 1999.

[16] Edwards, J. R., "A Low-Diffusion Flux-Splitting Scheme for Navier–Stokes Calculations," *Computers and Fluids*, Vol. 26, No. 6, 1997, pp. 635–659.

[17] Menter, F. R., "Zonal Two Equation k-omega Model for Aerodynamic Flows," AIAA Paper 93-2906, July 1993.

[18] Wilcox, D. C., "Wall Matching, a Rational Alternative to Wall Functions," AIAA Paper 89-0611, Jan. 1989.

[19] Pulliam, T. H., and Chaussee, D. S., "A Diagonal Form of an Implicit Approximate-Factorization Algorithm," *Journal of Computational Physics*, Vol. 39, No. 2, 1981, pp. 347–363.